Insights into the origin of carbonaceous chondrite organics from their triple oxygen isotope composition

DOI:
10.1073/pnas.1808101115

Document Version
Accepted author manuscript

Insights into the origin of carbonaceous chondrite organics from their triple oxygen isotope composition

Romain Tartèse[a,*], Marc Chaussidon[b], Andrey Gurenko[c], Frédéric Delarue[d], François Robert[e]

[a]School of Earth and Environmental Sciences, The University of Manchester, Manchester, M13 9PL, UK.

[b]Institut de Physique du Globe de Paris (IPGP), Université Sorbonne-Paris-Cité, Université Paris Diderot, CNRS UMR 7154, Paris, France

[c]Centre de Recherches Pétrographiques et Géochimiques, UMR 7358, Université de Lorraine, 54501 Vandoeuvre-lès-Nancy, France.

[d]Sorbonne Université, UPMC, CNRS, EPHE, PSL, UMR 7619 METIS, 4 place Jussieu, F-75005 Paris, France.

[e]Institut de Minéralogie, de Physique des Matériaux et de Cosmochimie, Muséum National d'Histoire Naturelle, Sorbonne Universités, CNRS, UPMC & IRD, 75005 Paris, France

[*]corresponding author: romain.tartese@manchester.ac.uk – Tel: +44161 275 6908

Short title: O isotope composition of carbonaceous chondrite organics.

To be submitted to PNAS

Categories: Physical Sciences > Earth, Atmospheric, and Planetary Sciences

Abstract

Dust grains of organic matter were the main reservoir of C and N in the forming Solar System, and are thus considered as an essential ingredient for the emergence of life. Yet, the physical environment and the chemical mechanisms at the origin of these organic grains are still highly debated. In this study we report the first high precision triple oxygen isotope composition for insoluble organic matter isolated from three emblematic carbonaceous chondrites, Orgueil, Murchison, and Cold Bokkeveld. These results suggest that the O isotope composition of carbonaceous chondrite insoluble organic matter falls on a slope 1 correlation line in the triple oxygen isotope diagram. The lack of detectable mass-dependent O isotopic fractionation, indicated by the slope 1 line, suggest that the bulk of carbonaceous chondrite organics did not form on asteroidal parent bodies during low temperature hydrothermal events. On the other hand, these new O isotope data, together with the H and N isotope characteristics of insoluble organic matter, may indicate that parent bodies of different carbonaceous chondrite types largely accreted organics formed locally in the protosolar nebula, possibly by photochemical dissociation of C-rich precursors.

Keywords

Carbonaceous chondrites; Organic matter; Oxygen isotopes; Protosolar nebula; Secondary ion mass spectrometry.

Significance Statement

Refractory organic matter found in volatile-rich asteroidal materials essentially comprise the elements C, H, O, N and S, which are thought to be important building blocks for life. Characterizing the origin(s) of these organics thus constitutes a key step to constrain the origin of life on Earth and appraise the habitability potential of other worlds. Yet how and where these organics formed is still highly debated. In this study we have determined the oxygen isotope composition of refractory organics from two families of carbonaceous chondrites. These data suggest that these organics formed in the nascent Solar System, possibly through chemical reactions occurring in the disk surrounding the young Sun.

\body

Introduction

Type 1-2 carbonaceous chondrites (CC) contain several wt.% carbon that mostly occurs as small patches of organic matter (OM) dispersed in the fine-grained matrix (1). Because this OM possibly played a key role in the development of life on the early Earth, its molecular structure, and its chemical and isotopic compositions have been extensively investigated (see 2 and references therein for a recent review). Despite this profusion of structural, chemical, and isotopic information, the question of whether CC OM formed in the cold interstellar medium (e.g., 3-5), in the protosolar nebula (PSN) (e.g., 6-9), or is a product of organic synthesis during hydrothermalism on CC parent bodies (e.g., 10) remains highly debated, notably because the extent of chemical and isotopic alteration of OM during secondary processes on CC parent bodies is debated (11-15).

Oxygen is the third most abundant element in the Solar System and has three stable isotopes ^{16}O, ^{17}O and ^{18}O. Because different fractionation laws govern interplanetary and intraplanetary processes (e.g., 16), the oxygen three-isotope system can provide information that cannot be accessed using other two-isotope systems of light elements such as H, C and N. In planetary bodies, variations of the $^{17}O/^{16}O$ and $^{18}O/^{16}O$ ratios almost always obey the mass-dependent relationship $\delta^{17}O \sim 0.52 \times \delta^{18}O$[1], while oxygen isotope abundance variations between Solar System gas and solids are primarily governed by the mass-independent relationship $\delta^{17}O \sim 1.0 \times$

[1]this δ-notation represents deviations in parts per thousand (‰) of the $^{17,18}O/^{16}O$ ratios relative to those of the Standard Mean Ocean Water (SMOW), according to the equation $\delta^{17,18}O = [(^{17,18}O/^{16}O)_{sample}/(^{17,18}O/^{16}O)_{SMOW} - 1] \times 1000$).

$\delta^{18}O$ (15). Much of our understanding of how our Solar System formed and evolved is thus based on O isotope studies of meteoritic materials (e.g., 16-17), and this should apply to carbonaceous chondrite OM since it contains ~10-25 wt.% O (11-12).

However, determining the O isotope composition of OM is challenging since it tends to be intimately mixed with O-rich silicates and oxides at a nano- to micro-scale in carbonaceous chondrites (e.g., 18). Acid-maceration used to isolate the insoluble OM (IOM) fraction from whole rock samples removes most of the silicates but is less effective at dissolving sulfides and some refractory O-bearing oxides such as chromite, spinel, hibonite or corundum. Bulk pyrolysis O isotope analysis of IOM is thus susceptible to contamination by residual mineral inclusions. To constrain the triple O isotope composition of carbonaceous chondrite IOM, we integrate here high spatial resolution secondary ion mass spectrometry (SIMS) data obtained using NanoSIMS with high precision $^{17,18}O/^{16}O$ isotope ratios obtained using large geometry multi-collector IMS 1270/80 ion probes (referred as L-SIMS in the following). For each L-SIMS O isotope analysis, measurement of ^{28}Si, ^{32}S, and $^{56}Fe^{16}O$ intensities allowed a first order filtering of data for which the O signals were largely affected by contamination by residual silicate and/or oxide phases (see Methods for details). The results presented here constitute the first high precision triple O isotope estimates for IOM residues isolated from two emblematic carbonaceous chondrite falls, the Ivuna-type (CI) Orgueil meteorite and the Mighei-type (CM) Murchison meteorite.

Results

The $\delta^{17}O$ and $\delta^{18}O$ values measured by L-SIMS in the Orgueil, Murchison and Cold Bokkeveld IOM residues range between -23.3 ± 2.4 ‰ and +18.9 ± 2.4 ‰ and -18.0 ± 2.3 ‰ and +16.9 ±

2.3 ‰ (uncertainties reported at 2σ), respectively (Fig. 1 and SI Appendix, Table S1). Least square regression through all the data yields a line defined by $\delta^{17}O = 1.00 (\pm 0.14) \times \delta^{18}O - 3.78 (\pm 1.35)$ (95% confidence level, n = 36, $r^2 = 0.86$), which is indistinguishable from the relationship known as the carbonaceous chondrite anhydrous mineral (CCAM) line ($\delta^{17}O = 0.95 \times \delta^{18}O - 4.18$) (Fig. 1).

The NanoSIMS data allow determining O isotope ratios with larger uncertainties than those obtained by L-SIMS, but with higher spatial resolution, i.e., over region of interests (ROI) that can be selected from ion imaging to minimize the effect of residual oxides and/or silicates, located through analysis of ^{28}Si and $^{56}Fe^{16}O$ simultaneously with O isotopes. The NanoSIMS analyses obtained over 40 μm^2 areas in Murchison and Orgueil IOM residues show little ^{28}Si hotspots but more abundant micron size ^{16}O-enriched areas (Figs. 2 and S2). The ^{16}O hotspots are generally associated with $^{56}Fe^{16}O$ hotspots, suggesting that magnetite and/or chromite are the main mineral phases that have resisted acid-maceration treatments.

In terms of surface, these ^{16}O-enriched ROI represent 16-18 % and 12-21 % of the total 40 μm × 40 μm areas analyzed in Murchison and Orgueil, respectively, while pure IOM ROI, defined based on ^{16}O intensity maps (see Methods), comprise 21-31 % and 18-20 % of the Murchison and Orgueil analyzed areas, respectively (Fig. 3 and SI Appendix, Table S2). The processed NanoSIMS data indicate that the $\delta^{17,18}O$ values of the residual O-rich inclusions in Murchison tend to be *ca*. 20-40 ‰ lower than the $\delta^{17,18}O$ values obtained for O-rich inclusions in Orgueil (SI Appendix, Table S2 and Fig. S3). The $\delta^{17,18}O$ values obtained for Murchison pure IOM areas are

around 0 to +10 ‰, while Orgueil pure IOM areas tend to have higher $\delta^{17,18}O$ values around +10 to +30 ‰ (Fig. 1). Overall, the O isotope composition estimated for Murchison and Orgueil pure IOM using NanoSIMS are roughly consistent with the $^{17,18}O$-rich end of the trends defined by Murchison and Orgueil acid-residues L-SIMS data (Fig. 1).

Discussion

Assessing the level of contamination from residuals micro-inclusions in IOM

The main challenge in determining the O isotope composition of IOM isolated from carbonaceous chondrites is related to the presence of residual nano- to micro-inclusions that have resisted acid-maceration, as shown here by NanoSIMS imaging. The consistency between O isotope values estimated for pure IOM based on high resolution NanoSIMS analyses and the most $^{17,18}O$-rich compositions obtained by L-SIMS for Murchison and Orgueil acid-residues, respectively, suggest that the latter provide an accurate estimate for the O isotope composition of Murchison and Orgueil IOM. We thus consider here that the average values calculated from the two most $^{17,18}O$-rich compositions measured by L-SIMS on both Murchison and Orgueil provide us with the best estimates for the O isotope compositions of pure IOM end-members in these samples. This yields $\delta^{18}O = +4.7 \pm 7.7$ ‰ (2SD) and $\delta^{17}O = +2.9 \pm 10.3$ ‰ (2SD) for Murchison IOM and $\delta^{18}O = +16.6 \pm 0.8$ ‰ (2SD) and $\delta^{17}O = +17.0 \pm 5.2$ ‰ (2SD) for Orgueil IOM.

Figure 4 presents the results of mixing calculations, where O isotope compositions have been calculated for mixed compositions between the IOM $\delta^{17,18}O$ values calculated from the $^{17,18}O$-rich L-SIMS data for Murchison and Orgueil and the most negative $\delta^{17,18}O$ values measured in mineral phases in both Murchison (*ca*. -40‰ for spinel; 21) and Orgueil (*ca*. -10‰ for olivine;

22). These calculations show that up to ~50 % and ~80 % contamination of the Murchison and Orgueil O signals, respectively, by ^{16}O-rich residual mineral phases could explain the spread of $\delta^{17,18}$O values measured by L-SIMS (Fig. 4). Such levels of contamination are consistent with NanoSIMS data obtained over 40 μm^2 areas selected randomly in Murchison and Orgueil acid-residues (SI Appendix, Fig. S3). In addition, these calculations are also consistent with O-rich contaminants in Murchison being characterized by $\delta^{17,18}$O values *ca*. 20-40 ‰ lower than those of O-rich inclusions in Orgueil (SI Appendix, Table S2 and Fig. S3), even though it is not possible to estimate their true $\delta^{17,18}$O values corrected for NanoSIMS instrumental mass fractionation since their exact mineralogy was not determined.

Comparison of bulk and SIMS-derived oxygen isotope data

Because O-rich residual contaminants have lower $\delta^{17,18}$O values than IOM, it is important to note that the pure IOM O isotope compositions calculated from ^{17,18}O-rich L-SIMS analyses provide minimum estimates. The δ^{18}O and δ^{17}O values estimated for Orgueil IOM by L-SIMS (+16.6 ± 0.8 ‰ and +17.0 ± 5.2 ‰, respectively) are higher than the bulk δ^{18}O and δ^{17}O values determined by Halbout et al. (23) (+6.0 ± 0.8 ‰ and +3.4 ± 0.4 ‰, respectively), which may indicate that their O isotope ratios were also affected by contamination issues. On the other hand the δ^{18}O value estimated for Orgueil IOM by L-SIMS is in good agreement with the bulk δ^{18}O value of +14.5 ± 0.6 ‰ determined by Alexander et al. (11). For Murchison IOM, the δ^{18}O value calculated from L-SIMS analyses of +4.7 ± 7.7 ‰ (2SD) is lower than the bulk IOM δ^{18}O values of +13.8 ± 1.6 ‰ (n = 2, 2SD) determined by Alexander et al. (11-12). These authors take advantage of the oxidation of sulfides in air over several days to gradually remove them from

165 acid-residues (11). Modification of the O isotope composition of organic O-bearing chemical
166 functions during such oxidation of acid-residues in air may be a possibility to explain the
167 discrepancy between bulk and L-SIMS $\delta^{18}O$ values obtained for Murchison IOM, since
168 atmospheric O_2 has a $\delta^{18}O$ value of *ca*. +23-24 ‰ (24-25). It is also possible that our L-SIMS
169 $\delta^{18}O$ estimate for Murchison IOM does not correspond to pure IOM but to IOM still
170 contaminated by minute amounts of O-rich residual inclusions. At this stage it is not possible to
171 favor one of these two hypotheses over the other. Interestingly, $\delta^{18}O$ values obtained on CM
172 chondrite bulk IOM are characterized by much larger variations (from -3.7 ‰ in Essebi to +14.4
173 ‰ in Murchison, both meteorites being observed falls) compared to other chondrite types (11-
174 12), which may either be related to variable contamination issues of bulk analyses or indicate that
175 CM chondrites accreted IOM with variable O isotope compositions. Clearly, further bulk and *in*
176 *situ* investigations are required to fully explore this issue.
177
178 *Triple oxygen isotope constraints on the origin of carbonaceous chondrite IOM*
179 The O isotope compositions estimated for Murchison IOM ($\delta^{17,18}O$ = *ca*. +3-5 ‰) and Orgueil
180 IOM ($\delta^{17,18}O$ = *ca*. +17 ‰) fall on the slope 1 line in a $\delta^{17}O$ vs. $\delta^{18}O$ diagram (Fig. 5). As
181 highlighted by Alexander et al. (11), $\delta^{18}O$ values of the CI and CM chondrite IOM are similar to
182 those of their matrix component (Fig. 5). However, the bulk and matrix $\delta^{17}O$ values obtained in
183 CI chondrites appear to be lower compared to the $\delta^{17}O$ of Orgueil IOM (Fig. 5). These new
184 results, combined with the O isotope composition of CI-CM chondrite original anhydrous
185 silicates, of matrix silicates, and of primordial alteration waters (which are thought to be similar
186 for CI and CM chondrite parent bodies; 21, 26-29), thus seem to rule out scenarios in which the

O isotope composition of O-bearing functional groups in CI chondrite IOM resulted from O isotope exchange between organic precursors and silicate components during aqueous alteration on the CI chondrite parent body (Fig. 5). On the other hand, because of the larger uncertainty associated with the $\delta^{17,18}O$ estimates for Murchison IOM, its formation during hydrothermal alteration on the CM parent body cannot be totally excluded.

The limited existing O isotope dataset obtained on a handful of carbonaceous chondrite meteorites so far suggest that IOM in the CI chondrite Orgueil tends to be enriched in $^{17,18}O$ compared to IOM in the CM chondrite Murchison (Fig. 5). Interestingly, this relationship is consistent with the variations of average H and N isotope compositions in CM and CI IOM, where CI IOM is enriched in D and ^{15}N compared to CM IOM (11-12). The D and ^{15}N enrichments commonly observed in CC IOM have generally been attributed to low temperature processes (<150 K) such as ion-molecule reactions taking place in dense interstellar media or at the surface of the PSN. However, recent experimental studies focused on the IOM molecular structure (9, 39), its bulk D/H (40) and the occurrence of D/H hotspots (41), and its noble gas isotope signatures (9), have argued that CC IOM could be produced by photochemical reactions involving organic radicals and taking place in the PSN regions where solar UV irradiation would have induced dissociation of C_xH_y molecules. Experiments have shown that photochemical reactions can produce mass-independent O isotope anomalies (e.g., 42-44). One could thus postulate that the mass-independent isotopic fractionation of oxygen isotopes in CC IOM also resulted from chemical reactions involving radical chemistry of CHON-bearing species in the PSN. If correct, such an effect now remains to be experimentally documented in a setting relevant to organics formation.

Cosmochemical implications

The O isotope compositions estimated for CI-CM chondrite IOM fall on a slope 1 line in a $\delta^{17}O$ vs. $\delta^{18}O$ diagram, which, at a larger scale, describes the O isotope variations of most Solar System objects such as the Sun, high temperature phases (i.e., CAI and chondrules) formed during the first few million years of Solar System evolution, and terrestrial planets for example (Fig. 5). Yet, the origin of this slope 1 line in planetary materials is still unknown. A possible mechanism involves self-shielding of ^{16}O-rich CO gas by UV light during photo-dissociation (e.g., 42), but whether this occurred in the presolar molecular cloud (45) or in the PSN (46) remains debated. O isotope compositions of CC IOM appear to fall on a slope 1 line; it could thus be argued that oxygen contained in CC IOM derived from a combination of that found in ^{16}O-rich CO and $^{17,18}O$-rich H_2O molecules formed as a result of self-shielding. If the different CC parent bodies accreted IOM sourced from a common carbonaceous reservoir, formed in the presolar molecular cloud, one may expect the various asteroidal parent bodies to have accreted presolar IOM grains characterized by similar O isotope compositions. The different triple O isotope compositions for Orgueil and Murchison IOM, dispersed along the slope 1 line, do not seem to favor such a scenario. Alternatively, and considering that Murchison and Orgueil IOM O isotope compositions are representative of those of CM and CI IOM in general, the observation that $\delta^{17,18}O_{CM\ IOM} < \delta^{17,18}O_{CI\ IOM}$, consistently with what has been measured for H and N isotope data ($\delta D_{CM\ IOM} < \delta D_{CI\ IOM}$ and $\delta^{15}N_{CM\ IOM} < \delta^{15}N_{CI\ IOM}$; 11-12), may indicate that carbonaceous asteroids accreted IOM that formed locally in the PSN through photochemical radical chemistry involving CHON-bearing species (9, 41). Because of its elevated δD and $\delta^{15}N$ values, it has been proposed that CR IOM could represent the least processed IOM component accreted in

carbonaceous asteroids (see discussion in ref. 2). Based on the observed relationship between H, N and O isotope compositions in CI and CM chondrite IOM, we would expect CR chondrite IOM to have $\delta^{17,18}O$ values higher than those of CI chondrite IOM. Determining with high precision the triple O isotope composition of CR chondrite IOM would thus provide important constraints to further explore the formation mechanism(s) of carbonaceous chondrite IOM.

Materials and Methods

Organic matter isolation

IOM was isolated from the Orgueil, Murchison, and Cold Bokkeveld carbonaceous chondrite meteorites through successive demineralization using a HF-HCl acidic treatment (47). Powdered meteorite samples were first stirred at room temperature in water, followed by CH_2Cl_2/MeOH (2/1, v/v), in order to remove soluble organic compounds. Carbonates were then removed at room temperature using HCl 6N to minimize the formation of fluorides during HF/HCl maceration. Samples were then centrifuged and washed with distilled water until reaching neutrality. Isolation of IOM was achieved through acid maceration at room temperature in a HF/HCl mixture (2/1, v/v). Samples were further centrifuged and washed with distilled water to reach neutrality. Neoformed fluorides were then degraded using HCl 6N at 60°C for 24 hours. After HCl hot acid maceration, IOM residues were washed with distilled water until reaching neutrality and thoroughly dried. For secondary ion mass spectrometry (SIMS) investigations, a few mg of IOM samples were pressed into high purity indium (99.999 %) and carbon coated.

IMS 1270/80 secondary ion mass spectrometry

Triple O isotope compositions of the IOM samples were measured using the CAMECA IMS 1270 E7 and 1280 HR2 ion probe instruments at the Centre de Recherches Pétrographiques et Géochimiques (CRPG) in Nancy (France) over several analytical sessions, using identical analytical protocols. Negative $^{16}O^-$, $^{17}O^-$ and $^{18}O^-$ secondary ions produced using a ~10 nA Cs^+ primary beam, accelerated at 10 kV and rastered over ~20 μm diameter areas, were measured in multicollection mode with one Faraday cup (FC) on the L'2 trolley for $^{16}O^-$ and two electron

multipliers (EM) for $^{17}O^-$ (central EM) and $^{18}O^-$ (H2 EM). To maximize peak flatness, entrance and exit slits were adjusted to achieve a mass resolving power of ~8000 for $^{17}O^-$ on the central EM and ~2500 on the off-axis L'2 FC and H2 EM (using slit #1 of the off-axis collectors). Organic matter samples contain significant amounts of OH (average $^{16}OH^-/^{17}O^-$ ~ 97 ± 17, ~120 ± 31 and ~121 ± 20 in Orgueil IOM, Murchison IOM and Cold Bokkeveld IOM, respectively) and the protocol used did not completely eliminate contribution from the $^{16}OH^-$ tail on the $^{17}O^-$ peaks. To quantify this contribution and adequately correct the measured $^{17}O/^{16}O$ ratios, we assumed that the $^{16}OH^-$ peak was symmetrical, calculated the mass difference between the center of the $^{17}O^-$ (16.9991 amu) and $^{16}OH^-$ (17.0027 amu) peaks and counted the $^{16}OH^-$ tail intensity at mass 17.0063 amu (mass $^{16}OH^-$ + [mass$^{16}OH^-$ - mass $^{17}O^-$]) for 50 s before and after each analysis. The $^{16}OH^-$ tail/peak ratios were ~$1.5 \pm 0.5 \times 10^{-5}$ in Murchison IOM, ~$1.1 \pm 0.1 \times 10^{-5}$ in Cold Bokkeveld and ~$1.9 \pm 0.5 \times 10^{-5}$ in Orgueil IOM. This resulted in correction of the measured $\delta^{17}O$ values by 0.7-2.8 ‰ in Murchison IOM, 1.3-1.8 ‰ in Cold Bokkeveld IOM and 0.8-2.4 ‰ in Orgueil IOM (SI Appendix, Table S1). For each analysis, the FC background was measured during pre-sputtering. Deadtime of the EM was also calibrated once per analytical session. The total analysis time was 260 s (60 s pre-sputtering and 40 cycles of 5 s each measurement time). Instrumental mass fractionation (IMF) for O isotope measurements in IOM samples was corrected by repeated analyses of our Clarno kerogen standard ($\delta^{18}O_{bulk}$ = 14.3 ± 0.1 ‰; 48), for which we assumed a $\delta^{17}O_{bulk}$ of 7.4 ‰, i.e., a terrestrial O isotope composition. Count rates obtained on the Clarno kerogen standard were 0.3-1.2 × 10^7 cps nA^{-1} for $^{16}O^-$, 1.1-4.5 × 10^3 cps nA^{-1} for $^{17}O^-$ and 0.6-2.3 × 10^4 cps nA^{-1} for $^{18}O^-$, similar to those obtained on the IOM samples (0.3-3.1 × 10^7 cps nA^{-1} for $^{16}O^-$, 0.1-1.1 × 10^4 cps nA^{-1} for $^{17}O^-$ and 0.5-5.5 × 10^4 cps nA^{-1} for $^{18}O^-$). The final uncertainties for individual $\delta^{17,18}O$ values, reported in SI Appendix (SI Appendix, Table S1) at the 2σ level, include uncertainties related to counting statistics associated with each individual analysis and the external reproducibility measured for $\delta^{17,18}O$ values on the Clarno kerogen standard. Over three analytical sessions in February 2016, July 2016 and December 2016, we obtained a weighted average $\Delta^{17}O$ of -0.1 ± 0.4 ‰ (95% confidence level, n = 66, MSWD = 3.0) (SI Appendix, Fig. S1). We further tested our analytical protocol on the Silurian Zdanow terrestrial kerogen and obtained an average $\delta^{18}O_{SIMS}$ of 12.4 ± 4.6 ‰ (2SD – n = 9), which is consistent with its bulk $\delta^{18}O$ of 13.4 ± 0.2 ‰ (48). The $\Delta^{17}O$ measured on Zdanow was

0.2 ± 1.8 ‰ (2SD – n = 9), indicating that Zdanow sits on the TFL, which shows that our L-SIMS protocol accurately measures the triple O isotope composition of organic residues.

The secondary species $^{12}C^{1}H$, ^{16}O, ^{28}Si, ^{32}S and $^{56}Fe^{16}O$ were collected following O isotope analyses on the same analytical spots using the magnetic peak switching mode and a ~10 nA Cs^+ beam in order to identify and filter the IOM data largely affected by contamination by residual silicate and oxide phases (see details in refs. 48-49).

Nanoscale secondary ion mass spectrometry

The triple O isotope composition of the Orgueil and Murchison IOM residues was also measured using the CAMECA NanoSIMS 50L ion probe instrument at The University of Manchester (UK). Negative $^{16}O^-$, $^{17}O^-$, $^{18}O^-$, $^{12}C_2^-$, $^{12}C_2{}^{14}N^-$, $^{28}Si^-$ and $^{56}Fe^{16}O^-$ secondary ion species produced using a ~15 pA Cs^+ primary beam, accelerated at 16 kV and rastered over 40 μm × 40 μm areas, were measured in multicollection mode on seven electron multipliers (EM). Before analysis, a ~100 pA Cs^+ primary beam was rastered over 50 μm × 50 μm areas for 5 minutes to clean the sample surface and reach sputtering equilibrium. To limit the $^{16}OH^-$ interference on the $^{17}O^-$ peak, a 10 μm wide entrance slit (ES5) was used at the entrance of the mass analyzer, and a 150 μm wide aperture slit (AS3) reduced the beam divergence, resulting in a mass resolving power of ~8000. An electron gun was used for charge compensation. Using these conditions, the count rates were 15000-35000 cps for ^{16}O, 500-1800 cps for $^{12}C_2$, 3000-10000 cps for $^{12}C^{14}N$ and 5-20 cps for $^{56}Fe^{16}O$, ensuring no detector ageing over the week-long analytical session. During the session, the vacuum in the analysis chamber remained constant at ~ 3×10^{-10} mbar. For data acquisition, the 40 μm^2 areas were divided in 256 × 256 pixels and between 320 and 600 frames were acquired at 1000 μs/px, resulting in a total analysis time of 6 to 11 hours per analysis. Automatic alignment of the secondary beam (EOS, Cy, and P2/P3) and of the peak positions was performed every 50 frames during each analysis based on scanning the $^{16}O^-$ peak. IMF for O isotope measurements in IOM samples was corrected by analyzing the same Clarno kerogen standard used for the L-SIMS analyses (see above). The final uncertainties for individual $\delta^{17,18}O$ values, reported in SI Appendix (SI Appendix, Table S2) at the 2σ level, include those related to counting statistics for each individual analysis and the external reproducibility measured for

$\delta^{17,18}O$ on the Clarno kerogen standard (±11.1 ‰ and ±11.9 ‰ for $\delta^{18}O$ and $\delta^{17}O$, respectively; 2SE, n = 3).

The NanoSIMS data were processed offline using the l'Image software package (L. Nittler, Carnegie Institution of Washington). A 44 ns deadtime was applied to all EM, and individual frames were binned into packages of 6-10 frames for each analysis to handle these large dataset more easily. Regions of interest (ROI) were defined using lower and upper thresholds for the different species, and comprised, for each analysis, the whole analyzed area, an area with intermediate ^{16}O intensity and a ^{16}O-rich area corresponding to hotspots. A ROI of 'pure IOM' was then defined by subtracting the ROI corresponding to the area with intermediate ^{16}O intensity to the ROI corresponding to the whole analyzed area. The $^{17}O/^{16}O$, $^{18}O/^{16}O$, $^{12}C^{14}N/^{12}C_2$ and $^{16}O/^{12}C_2$ ratios were calculated using l'Image.

All processed data are given in SI Appendix (SI Appendix, Tables S1 and S2). Raw data can be requested to the corresponding author.

Acknowledgments

We thank S. Derenne for providing the Murchison IOM sample, N. Bouden and J. Villeneuve for their help with L-SIMS analyses in Nancy, and I.C. Lyon for his help with NanoSIMS analyses in Manchester. We also thank the anonymous referees for their constructive reviews. This is IPGP contribution #XXXX and CRPG contribution #XXXX.

Funding: This work was supported by the ERC grant PaleoNanoLife (No. 290861; PI F. Robert), the ANR grant CRADLE (ANR-15-CE31-0004-01; PI M. Chaussidon), and the UK Science and Technology Facilities Council grants No. ST/M001253/1 (project Co-I I.C. Lyon) and ST/P005225/1 (PI R. Tartèse). The NanoSIMS at the University of Manchester was funded by UK Research Partnership Investment Funding (UKRPIF) Manchester RPIF Round 2.

References

1. Hayes JM (1967) Organic constituents of meteorites – a review. *Geochim Cosmochim Acta* 31:1395-1440.
2. Alexander CMO'D, Cody GD, De Gregorio BT, Nittler LR, Stroud RM (2017) The nature, origin and modification of insoluble organic matter in chondrites, the major source of Earth's C and N. *Chem Erde Geochem* 77:227-256.
3. Robert F, Epstein S (1982) The concentration and isotopic composition of hydrogen, carbon and nitrogen in carbonaceous meteorites. *Geochim Cosmochim Acta* 46:81-95.
4. Yang J, Epstein S (1983) Interstellar organic matter in meteorites. *Geochim Cosmochim Acta* 47:2199-2216.
5. Busemann H, et al. (2006) Interstellar chemistry recorded in organic matter from primitive meteorites. *Science* 312:727-730.
6. Remusat L, Palhol F, Robert F, Derenne S, France-Lanord C (2006) Enrichment of deuterium in insoluble organic matter from primitive meteorites: a solar system origin? *Earth Planet Sci Lett* 243:15-25.
7. Gourier D, et al. (2008) Extreme deuterium enrichment of organic radicals in the Orgueil meteorite: revisiting the interstellar interpretation? *Geochim Cosmochim Acta* 72:1914-1923.
8. Derenne S, Robert F (2010) Model of molecular structure of the insoluble organic matter isolated from Murchison meteorite. *Meteorit Planet Sci* 45:1461-1475.
9. Kuga M, Marty B, Marrocchi Y, Tissandier L (2015) Synthesis of refractory organic matter in the ionized gas phase of the solar nebula. *Proc Natl Acad Sci USA* 112:7129-7134.
10. Cody GD, et al. (2011) Establishing a molecular relationship between chondritic and cometary organic solids. *Proc Natl Acad Sci USA* 108:19171-19176.
11. Alexander CMO'D, Fogel M, Yabuta H, Cody GD (2007) The origin and evolution of chondrites recorded in the elemental and isotopic compositions of their macromolecular organic matter. *Geochim Cosmochim Acta* 71:4380-4403.
12. Alexander CMO'D, et al. (2010) Deuterium enrichments in chondritic macromolecular material – implications for the origin and evolution of organics, water and asteroids. *Geochim Cosmochim Acta* 74:4417-4437.
13. Orthous-Daunay FR, et al. (2013) Mid-infrared study of the molecular structure variability of insoluble organic matter from primitive chondrites. *Icarus* 223:534-543.
14. Quirico E, et al. (2014) Origin of insoluble organic matter in type 1 and 2 chondrites: New clues, new questions. *Geochim Cosmochim Acta* 136:80-99.
15. Hashiguchi M, Kobayashi S, Yurimoto H (2015) Deuterium- and ^{15}N-signatures of organic globules in Murchison and Northwest Africa 801 meteorites. *Geochem J* 49:377-391.
16. Clayton RN (1993) Oxygen isotopes in meteorites. *Ann Rev Earth Planet Sci* 21:115-149.
17. McKeegan KD, et al. (2011) The oxygen isotopic composition of the Sun inferred from captured solar wind. *Science* 332:1528-1532.

18. Le Guillou C, Bernard S, Brearley AJ, Remusat L (2014) Evolution of organic matter in Orgueil, Murchison and Renazzo during parent body aqueous alteration: *In situ* investigations. *Geochim Cosmochim Acta* 131:368-392.
19. Clayton RN, Onuma N, Grossman L, Mayeda TK (1977) Distribution of the presolar component in Allende and other carbonaceous chondrites. *Earth Planet Sci Lett* 34:209-224.
20. Young ED, Russell SS (1998) Oxygen reservoirs in the early solar nebula inferred from an Allende CAI. *Science* 282:452-455.
21. Clayton RN, Mayeda TK (1984) The oxygen isotope record in Murchison and other carbonaceous chondrites. *Earth Planet Sci Lett* 67:151-161.
22. Leshin LA, Rubin AE, McKeegan KD (1997) The oxygen isotopic composition of olivine and pyroxene from CI chondrites. *Geochim Cosmochim Acta* 61:835-845.
23. Halbout J, Robert F, Javoy M (1990) Hydrogen and oxygen isotope compositions in kerogen from the Orgueil meteorite: Clues to a solar origin. *Geochim Cosmochim Acta* 54:1453-1462.
24. Kroopnick P, Craig H (1972) Atmospheric oxygen: Isotopic composition and solubility fractionation. *Science* 175:54-55.
25. Luz B, Barkan E (2011) The isotopic composition of atmospheric oxygen. *Global Biogeochem Cycles* 25:GB3001, doi:10.1029/2010GB003883.
26. Rowe MW, Clayton RN, Mayeda TK (1994) Oxygen isotopes in separated components of CI and CM meteorites. *Geochim Cosmochim Acta* 58:5341-5347.
27. Clayton RN, Mayeda TK (1999) Oxygen isotope studies of carbonaceous chondrites. *Geochim Cosmochim Acta* 63:2089-2104.
28. Fujiya W (2018) Oxygen isotopic ratios of primordial water in carbonaceous chondrites. *Earth Planet Sci Lett* 481:264-272.
29. Marrocchi Y, Bekaert DV, Piani L (2018) Origin and abundance of water in carbonaceous asteroids. *Earth Planet Sci Lett* 482:23-32.
30. Aléon J, El Goresy A, Zinner E (2007) Oxygen isotope heterogeneities in the earliest protosolar gas recorded in a meteoritic calcium–aluminum-rich inclusion. *Earth Planet Sci Lett* 263:114-127.
31. Krot AN, et al. (2008) Oxygen isotopic compositions of Allende Type C CAIs: Evidence for isotopic exchange during nebular melting and asteroidal metamorphism. *Geochim Cosmochim Acta* 72:2534-2555.
32. Bodénan JD, Starkey NA, Russell SS, Wright IP, Franchi IA (2014) An oxygen isotope study of Wark-Lovering rims on type A CAIs in primitive carbonaceous chondrites. Earth Planet Sci Lett 401:327-336.
33. Clayton RN, et al. (1983) Oxygen isotopic compositions of chondrules in Allende and ordinary chondrites. *Chondrules and Their Origins*, ed King EA (Lunar and Planetary Institute, Houston), pp 37-43.
34. Rubin AE, Wasson JT, Clayton RN, Mayeda TK (1990) Oxygen isotopes in chondrules and coarse-grained chondrule rims from the Allende meteorite. *Earth Planet Sci Lett* 96:247-255.

35. Weisberg MK, Prinz M, Clayton RN, Mayeda TK (1993) The CR (Renazzo-type) carbonaceous chondrite group and its implications. *Geochim Cosmochim Acta* 57:1567-1586.
36. Jones RH, et al. (2004) Oxygen isotope heterogeneity in chondrules from the Mokoia CV3 carbonaceous chondrite. *Geochim Cosmochim Acta* 68:3423-3438.
37. Jenniskens P, et al. (2012) Radar-enabled recovery of the Sutter's Mill meteorite, a carbonaceous chondrite regolith breccia. *Science* 6114:1583-1587.
38. Verdier-Paoletti MJ, et al. (2017) Oxygen isotope constraints on the alteration temperatures of CM chondrites. Earth Planet Sci Lett 458:273-281.
39. Biron K, Derenne S, Robert F, Rouzaud JN (2015) Toward an experimental synthesis of the chondritic insoluble organic matter. *Meteorit Planet Sci* 50:1408-1422.
40. Laurent B, et al. (2015) The deuterium/hydrogen distribution in chondritic organic matter attests to early ionizing irradiation. *Nat Comm* 6:8567, doi:10.1038/ncomms9567.
41. Robert F, et al. (2017) Hydrogen isotope fractionation in methane plasma. *Proc Natl Acad Sci USA* 114:870-874.
42. Thiemens MH, Heidenreich JE III (1983) The mass-independent fractionation of oxygen – a novel isotope effect and its possible cosmochemical implications. *Science* 219:1073-1075.
43. Chakraborty S, Ahmed M, Jackson TL, Thiemens MH (2008) Experimental test of self-shielding in vacuum ultraviolet photodissociation of CO. *Science* 321:1328-1331.
44. Chakraborty S, Yanchulova P, Thiemens MH (2013) Mass-independent oxygen isotopic partitioning during gas-phase SiO_2 formation. *Science* 342:463-466.
45. Yurimoto H, Kuramoto K (2004) Molecular cloud origin for the oxygen isotope heterogeneity in the solar system. *Science* 305:1763-1766.
46. Lyons JR, Young ED (2005) CO self-shielding as the origin of oxygen isotope anomalies in the early solar nebula. *Nature* 435:317-320.
47. Durand B, Nicaise G (1980) Procedures for kerogen isolation. *Kerogen – Insoluble organic matter from sedimentary rocks*, ed Durand B (Technip, Paris), pp 35-54.
48. Tartèse R, Chaussidon M, Gurenko A, Delarue F, Robert F (2016) *In situ* oxygen isotope analysis of fossil organic matter. *Geochim Cosmochim Acta* 182:24-39.
49. Tartèse R, Chaussidon M, Gurenko A, Delarue F, Robert F (2017) Warm Archean oceans reconstructed from oxygen isotope composition of early-life remnants. *Geochem Perspect Lett* 3:55-65.

Figure captions

Figure 1: $\delta^{17,18}O$ values obtained in Orgueil, Murchison and Cold Bokkeveld IOM residues. The terrestrial fractionation line (TFL), the carbonaceous chondrite anhydrous mineral line (CCAM; 19) and the Young and Russell line (Y&R; 20) are also represented.

Figure 2: NanoSIMS images showing the distribution of $^{12}C^{14}N$, ^{16}O, $^{56}Fe^{16}O$ and ^{28}Si secondary ion species in Murchison and Orgueil IOM acid-maceration residues. White and cyan arrows indicate higher $^{56}Fe^{16}O$ and ^{28}Si intensities, respectively.

Figure3: Examples of the regions of interest defined on ^{16}O ion images for one analysis each of Murchison and Orgueil acid-residues. ROI#3 (left) correspond to intermediate O intensity, ROI#4 (center) correspond to O hotspots, and ROI#5 (right) correspond to pure IOM (see text for details).

Figure 4: Calculated O isotope values for mixed compositions between the estimated IOM $\delta^{17,18}O$ values (grey stars) in (A) Murchison and (B) Orgueil acid-residues and the most negative $\delta^{17,18}O$ values measured in mineral phases in both Murchison (*ca*. -40‰ for spinel; 21) and Orgueil (*ca*. -10‰ for olivine; 22) (dark grey hexagons). White dots represent 10% mixing intervals, and 20% mixing intervals are given on the diagrams from 0% to 100% mineral contribution.

Figure 5: O isotope compositions measured by L-SIMS on IOM residues isolated from the Orgueil and Murchison carbonaceous chondrites. The terrestrial fractionation line (TFL), the CCAM line, and the Y&R line, are also represented, together with the O isotope compositions of the Sun (17), of CI and CM chondrite components (bulk, matrix and anhydrous silicates; 21-22, 26-27), of carbonaceous chondrite Ca- and Al-rich inclusions (30-32), chondrules (33-37) and carbonates (38). Estimates for the O isotope composition of CM chondrite primordial water (HW1 & HW2) are from ref. 27 for HW1 and ref. 38 for HW2.

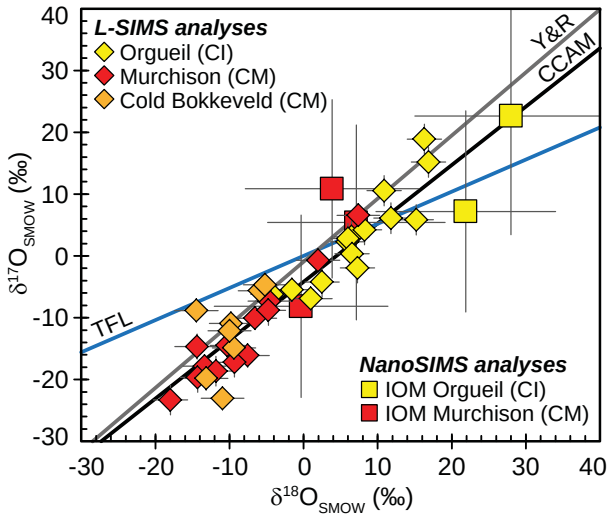
L-SIMS analyses
Orgueil (CI)
Murchison (CM)
Cold Bokkeveld (CM)
NanoSIMS analyses
IOM Orgueil (CI)
IOM Murchison (CM)
Y&R
CCAM
TFL
δ17OSMOW (‰)
δ18OSMOW (‰)
40
30
20
10
0
-10
-20
-30
-30
-20
-10
0
10
20
30
40

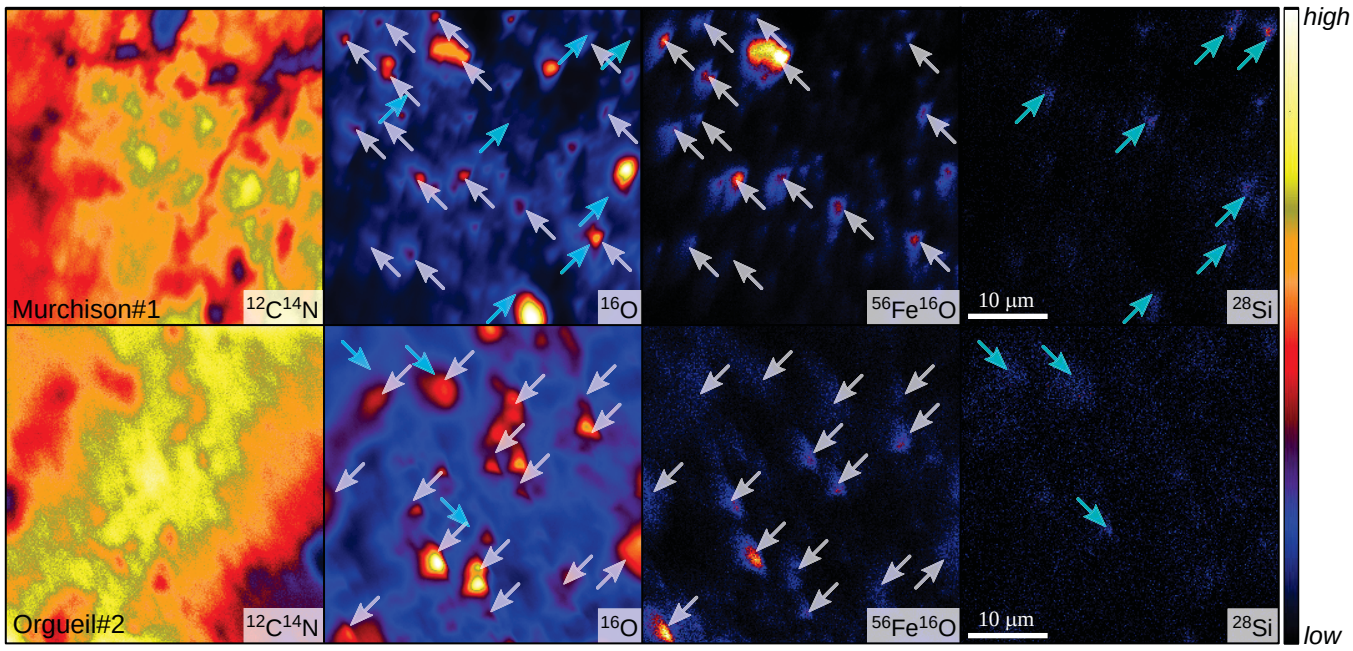
Murchison#1
$^{12}C^{14}N$
^{16}O
$^{56}Fe^{16}O$
10 µm
^{28}Si
Orgueil#2
$^{12}C^{14}N$
^{16}O
$^{56}Fe^{16}O$
10 µm
^{28}Si
high
low

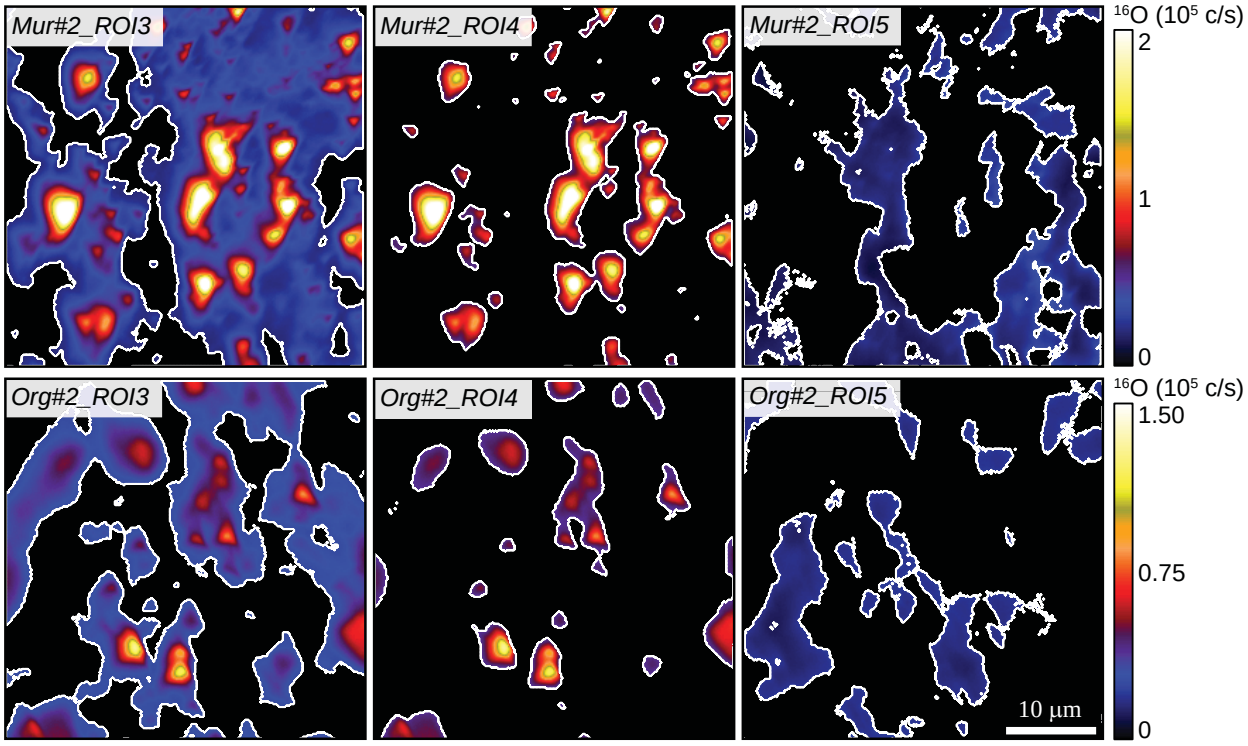
Mur#2_ROI3
Mur#2_ROI4
Mur#2_ROI5
^{16}O (10^5 c/s)
2
1
0
Org#2_ROI3
Org#2_ROI4
Org#2_ROI5
^{16}O (10^5 c/s)
1.50
0.75
0
10 µm

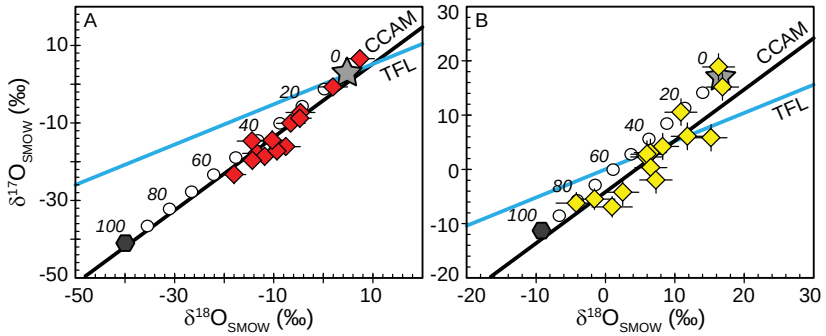
A
B
CCAM
TFL
0
20
40
60
80
100
10
-10
-30
-50
30
20
0
-20
-50
-30
-10
10
-20
-10
0
10
20
30
δ17OSMOW (‰)
δ18OSMOW (‰)

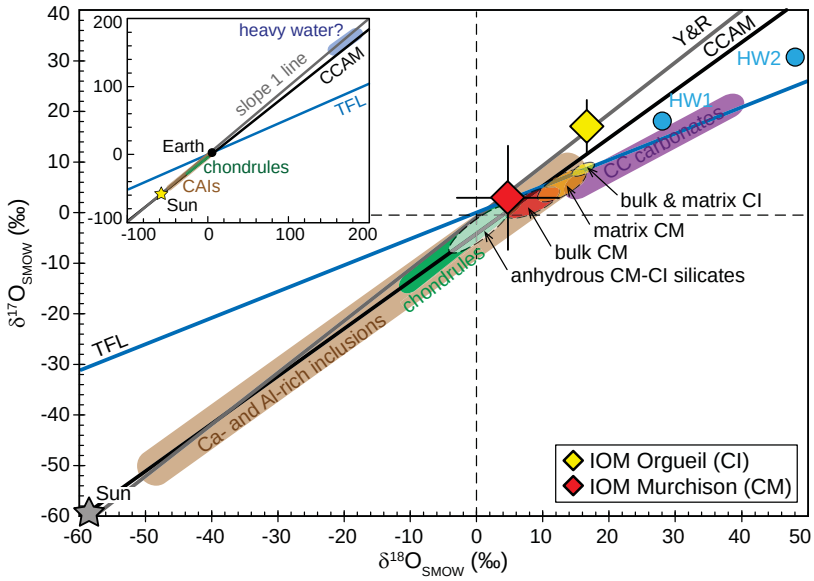
heavy water?
slope 1 line
CCAM
TFL
Earth
chondrules
CAIs
Sun
Y&R
CCAM
HW2
HW1
CC carbonates
bulk & matrix CI
matrix CM
bulk CM
anhydrous CM-CI silicates
chondrules
Ca- and Al-rich inclusions
TFL
Sun
IOM Orgueil (CI)
IOM Murchison (CM)
δ17OSMOW (‰)
δ18OSMOW (‰)

PNAS
www.pnas.org

Supplementary Information for

Insights into the origin of carbonaceous chondrite organics from their triple oxygen isotope composition

R. Tartèse, M. Chaussidon, A. Gurenko, F. Delarue, F. Robert

Corresponding author: Romain Tartèse
Email: romain.tartese@manchester.ac.uk

This PDF file includes:

Figs. S1 to S3
Tables S1 to S2

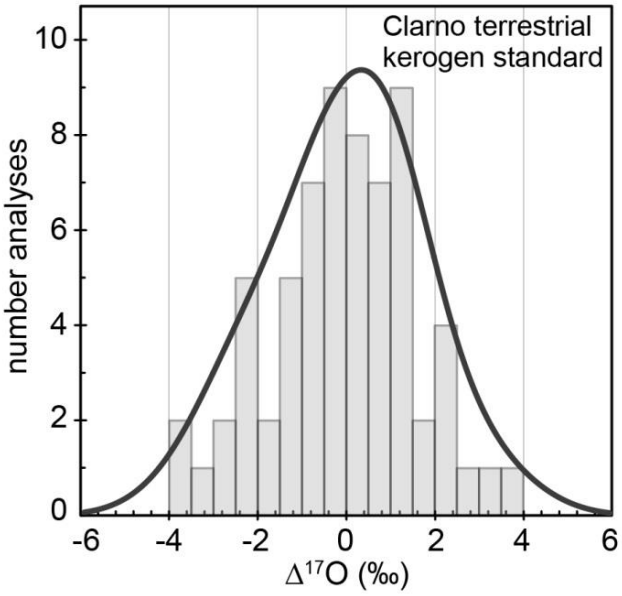

Fig. S1. Histogram and probability distribution of $\Delta^{17}O$ values measured on the Clarno kerogen standard over all the L-SIMS analytical sessions.

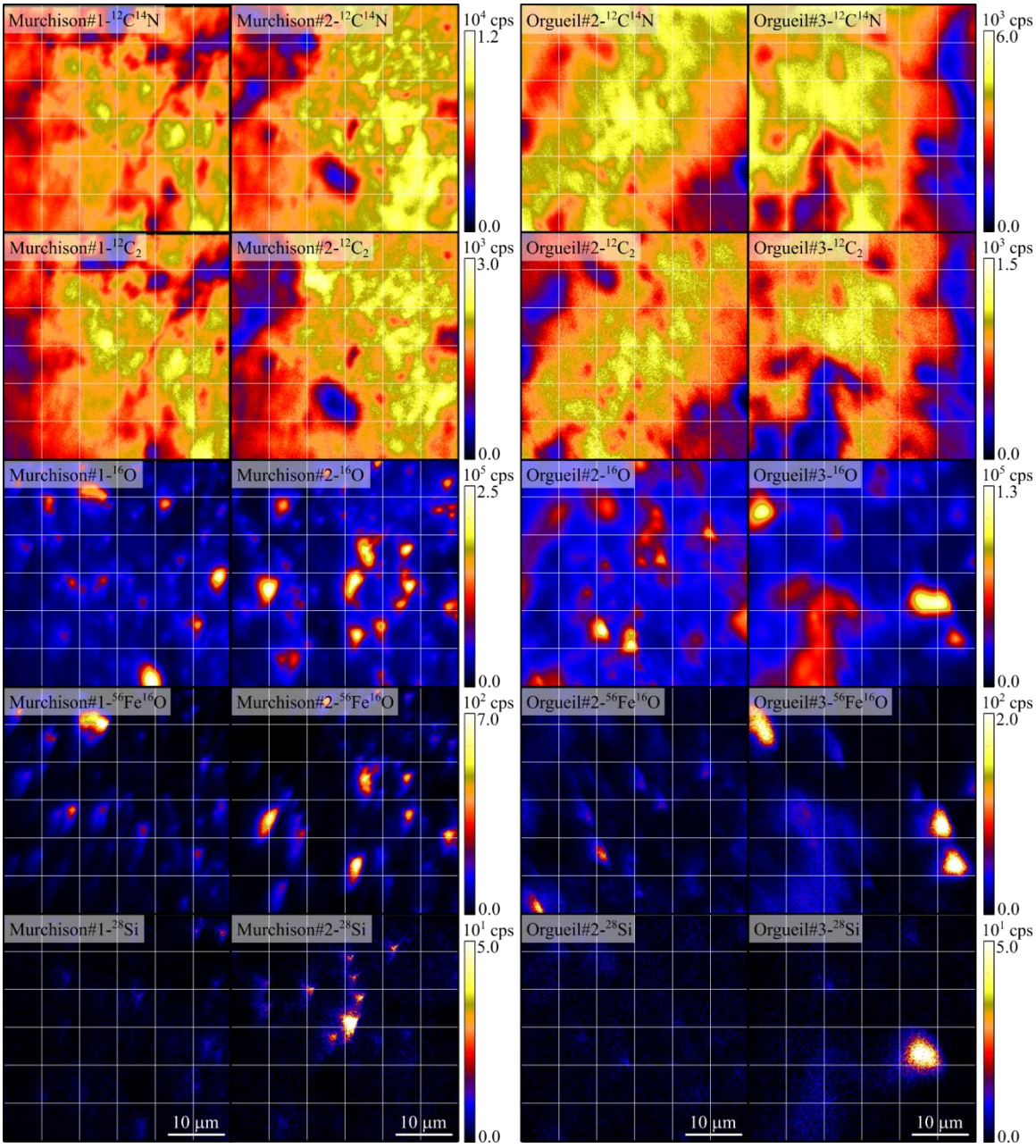

Fig. S2. NanoSIMS images obtained on 40 × 40 µm areas in Murchison and Orgueil IOM showing the distribution of $^{12}C^{14}N$, $^{12}C_2$, ^{16}O, $^{56}Fe^{16}O$ and ^{28}Si secondary ion species.

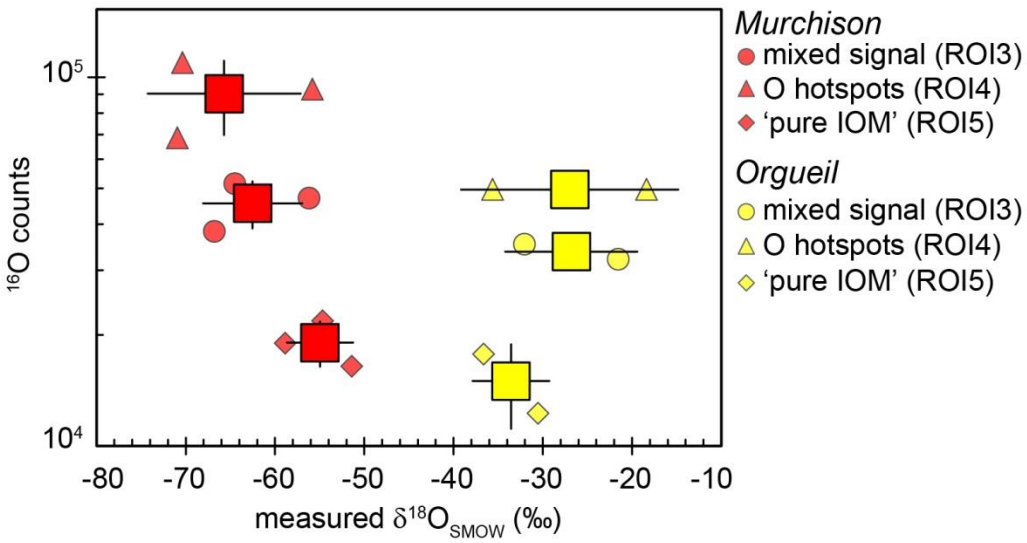

Fig. S3. Plot showing the NanoSIMS ^{16}O intensity versus the measured $\delta^{18}O$ values for regions of interest corresponding to areas with a mixture of IOM and O-rich residual minerals (ROI3), O-rich hotspots (ROI4), and 'pure IOM' areas (ROI5) for five areas analyzed in Murchison and Orgueil acid-residues.

Table S1. L-SIMS oxygen isotope results. *Indicates the contribution of the $^{16}OH^-$ peak tail on the measured $^{17}O^-$ intensity.

Analysis	Secondary ion intensity (cps nA^{-1} primary current)			^{16}OH (‰)*	Isotope ratios (‰ vs. SMOW)					
	$^{16}O^-$	$^{17}O^-$	$^{18}O^-$		$\delta^{18}O$	2σ	$\delta^{17}O$	2σ	$\Delta^{17}O$	2σ
Orgueil IOM										
Orgueil_3iso@4	3.80E+06	1.40E+03	7.21E+03	1.7	-4.2	2.9	-6.2	2.0	-4.0	2.3
Orgueil_3iso@5	3.98E+06	1.47E+03	7.57E+03	1.3	-1.6	2.9	-5.5	1.9	-4.7	2.1
Orgueil_3iso@7	4.07E+06	1.50E+03	7.75E+03	0.8	1.0	2.9	-6.9	1.9	-7.4	1.9
Orgueil@2	3.02E+06	1.13E+03	5.82E+03	2.4	5.9	2.3	2.3	2.4	-0.8	2.2
Orgueil@3	2.56E+06	9.59E+02	4.94E+03	2.3	6.5	2.3	3.1	2.5	-0.3	2.5
Orgueil@4	2.33E+06	8.72E+02	4.49E+03	2.3	6.0	2.3	2.8	2.5	-0.3	2.5
Orgueil@5	6.27E+06	2.37E+03	1.21E+04	1.5	10.9	2.3	10.5	2.5	4.9	2.4
Orgueil@6	7.54E+06	2.87E+03	1.46E+04	1.5	16.3	2.3	18.9	2.4	10.4	2.2
Orgueil@9	4.10E+06	1.55E+03	7.99E+03	2.2	16.9	2.3	15.2	2.4	6.4	2.3
Orgueil@11	2.64E+06	9.92E+02	5.12E+03	2.0	11.8	2.3	6.1	2.5	0.0	2.5
Orgueil@12	4.28E+06	1.59E+03	8.22E+03	1.3	2.5	2.3	-4.2	2.4	-5.5	2.2
Orgueil@13	3.64E+06	1.37E+03	7.03E+03	1.4	8.2	2.3	4.2	2.4	-0.1	2.2
Orgueil@16	2.44E+06	9.12E+02	4.71E+03	1.8	6.5	2.3	0.3	2.5	-3.1	2.4
Orgueil@17	2.61E+06	9.79E+02	5.08E+03	1.7	15.2	2.3	5.8	2.4	-2.1	2.3
Orgueil@19	1.50E+07	5.57E+03	2.84E+04	2.1	7.3	2.3	-2.0	2.4	-5.7	2.3
Murchison IOM										
Murchison_3iso@1	2.57E+07	9.40E+03	4.71E+04	1.7	-6.5	2.9	-10.1	1.9	-6.7	1.7
Murchison_3iso@2	4.42E+07	1.61E+04	8.14E+04	0.7	-7.5	2.9	-16.1	1.9	-12.2	1.8
Murchison_3iso@3	2.55E+07	9.45E+03	4.81E+04	1.1	1.9	2.9	-0.7	1.9	-1.7	2.0
Murchison_3iso@4	9.77E+06	3.66E+03	1.86E+04	1.9	7.4	2.9	6.6	1.9	2.7	1.7
Murchison_3iso@5	3.05E+07	1.11E+04	5.53E+04	1.1	-13.4	2.9	-17.8	1.9	-10.9	1.7
Murchison_3iso@7	1.36E+07	4.96E+03	2.51E+04	1.5	-14.4	3.0	-14.7	2.0	-7.2	2.9
Murchison_3iso@8	1.55E+07	5.70E+03	2.89E+04	1.0	-4.6	2.9	-7.3	1.9	-4.9	1.8
Murchison@1	1.66E+07	6.10E+03	3.10E+04	2.8	-4.7	2.3	-8.8	2.4	-6.3	2.2
Murchison@2	1.42E+07	5.17E+03	2.64E+04	2.8	-18.0	2.3	-23.3	2.4	-14.0	2.2
Murchison@5	2.06E+07	7.51E+03	3.82E+04	1.9	-11.8	2.3	-18.6	2.4	-12.5	2.0
Murchison@6	1.34E+07	4.92E+03	2.52E+04	2.5	-9.3	2.3	-17.2	2.4	-12.4	2.1
Murchison@8	7.39E+06	2.73E+03	1.40E+04	4.9	-10.3	2.3	-14.5	2.5	-9.1	2.4
Murchison@9	1.73E+07	6.31E+03	3.21E+04	2.0	-14.3	2.3	-19.7	2.4	-12.2	2.2
Cold Bokkeveld IOM										
CB_3iso@1	1.41E+07	5.12E+03	2.61E+04	1.5	-13.1	2.9	-19.8	2.0	-13.0	2.3
CB_3iso@2	1.56E+07	5.70E+03	2.90E+04	1.4	-9.4	2.9	-14.9	2.0	-10.0	2.2
CB_3iso@3	1.11E+07	4.07E+03	2.06E+04	1.6	-14.5	2.9	-8.8	1.9	-1.3	2.0
CB_3iso@4	1.35E+07	4.91E+03	2.52E+04	1.3	-10.9	2.9	-23.0	1.9	-17.3	1.9
CB_3iso@5	1.20E+07	4.42E+03	2.24E+04	1.3	-9.8	2.9	-10.9	1.9	-5.8	1.7
CB_3iso@6	1.52E+07	5.59E+03	2.83E+04	1.3	-5.9	2.9	-5.6	1.9	-2.5	1.6
CB_3iso@7	8.59E+06	3.16E+03	1.61E+04	1.8	-10.0	2.9	-12.1	1.9	-6.9	1.9
CB_3iso@8	1.71E+07	6.32E+03	3.19E+04	1.1	-5.2	2.9	-4.7	1.9	-2.0	1.8

Table S2. NanoSIMS results obtained on Murchison and Orgueil acid-maceration residues.

ROI	Area (μm^2)	Intensity (cps)							Ratio (in ‰ vs. SMOW for $\delta^{17,18}O$)								IMF corrected (‰)			
		^{16}O	^{17}O	^{18}O	$^{12}C_2$	$^{12}C^{14}N$	^{28}Si	$^{56}Fe^{16}O$	$\delta^{18}O$	1σ	$\delta^{17}O$	1σ	$^{12}C^{14}N/^{12}C_2$	1σ	$^{16}O/^{12}C_2$	1σ	$\delta^{18}O$	2σ	$\delta^{17}O$	2σ
Murchison #1																				
All area	1517	31880	11.6	59.7	1607.5	6399.7	0.9	36.0	-65.7	0.6	-50.6	1.5	3.88	0.04	19.8	0.2				
Broad O rich	1091	38251	13.9	71.6	1704.2	6710.0	1.1	45.2	-66.8	0.7	-51.7	1.6	3.84	0.04	22.4	0.3				
O hotspot	270	68513	24.7	127.7	1591.3	6259.3	1.1	94.6	-70.9	1.0	-58.6	2.3	3.84	0.04	43.0	0.5				
'pure' IOM	314	18985	6.9	35.8	1736.2	6985.5	0.9	14.5	-58.8	1.9	-50.2	4.4	3.92	0.04	10.8	0.2	-0.3	11.7	-8.1	14.8
Murchison #2																				
All area	1529	39379	14.5	74.5	1669.1	7047.1	1.8	40.7	-56.6	0.7	-40.5	1.7	4.10	0.05	23.1	0.4				
Broad O rich	1191	47012	17.2	89.0	1772.4	7463.7	2.0	50.8	-56.2	0.8	-40.7	1.7	4.10	0.05	26.0	0.4				
O hotspot	268	92795	33.9	175.7	1688.2	7168.4	3.1	123.6	-55.8	1.1	-46.0	2.6	4.14	0.04	52.9	1.0				
'pure' IOM	475	21818	8.1	41.4	1833.6	7867.2	1.3	15.9	-54.7	1.8	-31.2	4.1	4.17	0.05	11.6	0.2	3.8	11.7	10.9	14.4
Murchison #3																				
All area	1548	38520	14.1	72.4	1550.8	7138.4	1.0	23.8	-62.6	1.0	-44.6	1.7	4.44	0.06	24.7	0.4				
Broad O rich	999	51440	18.8	96.5	1622.3	7371.6	1.1	32.2	-64.5	1.0	-45.9	1.9	4.39	0.05	31.6	0.4				
O hotspot	249	109608	39.7	204.4	1445.1	6530.8	1.0	64.9	-70.4	1.5	-53.0	2.5	4.37	0.05	76.4	0.7				
'pure' IOM	400	16439	6.1	31.3	1640.8	7863.2	0.8	9.7	-51.4	2.2	-36.7	5.2	4.64	0.05	9.5	0.2	7.1	12.0	5.4	15.8
Orgueil #3																				
All area	1548	27211	10.1	52.8	816.5	3682.9	1.3	9.8	-32.5	0.9	-35.0	2.0	4.27	0.07	33.2	0.4				
Broad O rich	745	35271	13.0	68.4	756.8	3574.5	1.5	13.2	-32.1	1.1	-34.2	2.5	4.47	0.07	46.4	0.6				
O hotspot	191	49642	18.3	96.0	672.7	3345.4	1.7	19.9	-35.6	1.8	-44.4	4.1	4.72	0.07	73.2	1.1				
'pure' IOM	314	17747	6.6	34.3	946.2	4072.3	1.1	5.4	-36.6	2.4	-34.9	5.6	4.08	0.07	18.6	0.2	21.9	12.2	7.2	16.3
Orgueil #4																				
All area	1531	23537	8.9	46.1	712.6	3273.8	2.0	15.3	-22.8	1.0	-12.3	2.3	4.26	0.09	32.1	0.6				
Broad O rich	901	32093	12.2	62.9	661.0	3333.3	2.9	23.1	-21.6	1.1	-12.2	2.5	4.65	0.11	48.0	0.8				
O hotspot	323	49644	18.9	97.8	465.2	2801.3	5.4	42.5	-18.4	1.5	-3.2	3.5	5.53	0.13	106.5	1.6				
'pure' IOM	272	12251	4.6	23.8	993.2	4146.7	0.7	3.8	-30.5	3.3	-19.5	7.5	3.89	0.08	11.5	0.3	28.0	13.0	22.6	19.2